Experimental investigation of the axial oxidizer injectors geometry on a 1-kN paraffin-fueled hybrid rocket motor

M. Bouziane [a],*, A.E.M. Bertoldi [b], P. Hendrick [c], M. Lefebvre [d]

[a] Laboratory of propulsion and reactive system, Ecole Militaire Polytechnique, BP 17 Bordj-El-Bahri, Alger, Algiers
[b] Faculty of Gama, University of Brasília, Área Especial de Indústria e Projeção A, 72444-240 Brasília, Brazil
[c] Aero-Thermo-Mechanics department, Université Libre de Bruxelles, F.D. Roosevelt Avenue 50, 1050 Brussels, Belgium
[d] Department of Chemistry, Royal Military Academy, Avenue de la Renaissance 30, 1000 Brussels, Belgium

ARTICLE INFO

ABSTRACT

The showerhead is the most common type of injector used in hybrid rocket motors due to its design and manufacture simplicity. The main drawback of the showerheads (SH) is the relatively low performance in terms of combustion efficiency because of the poor atomization of the liquid oxidizer. This study investigates the problem to enrich the technical literature by presenting detailed experimental data on showerhead injectors by a series of static firing tests using a 1-kN lab-scale hybrid rocket, applying four kinds of showerhead injectors, named SH1 (benchmark), SH2, SH3, and SH4. They differ from each other by the number, distribution, and dimension of the orifice elements. Main performance parameters such as fuel regression rate, specific impulse, and combustion efficiency are experimentally obtained.

Two different series of tests were carried out. At first, the influence of SH injector geometries was studied. The injectors SH2, SH3, and SH4 were used under the same initial conditions, and the results were compared with SH1. In the second set of tests, the SH4 injector was chosen, and the effects of the fuel grain initial port diameter were investigated. Using the data obtained in the second battery of tests was possible to determine the influence of the fuel port diameter on the motor efficiency and establish the regression rate law of nitrous oxidizer/paraffin-based fuel for this specific configuration.

1. Introduction

The development of hybrid propulsion systems based on hydrocarbons fuels is becoming a technology asset for small launchers and new generation space transportation systems. In particular, hybrid rocket motors based on N_2O/Wax or LOX/Wax are potential candidates for future transportation systems since they combine the advantages of both solid and liquid propulsion systems. Hybrid rocket motors are safe and low-cost, and they use half of the feed lines of the liquid rockets, preserving the operation flexibility. Contrary to typical solid rockets, they are a low explosive hazard [1–3]. While hybrid rockets inherit advantages from liquid and solid systems, there are also challenges to be overcome in order to advance the technology [4]. The main drawbacks of classical hybrid fuels are low regression rate of the solid fuel, poor combustion efficiency, and therefore a low specific impulse [3,5].

In a typical hybrid rocket motor configuration, the fuel is solid, and the oxidizer is liquid. A liquid oxidizer is injected in the form of a spray through an atomizer. In ideal cases, it vaporizes and reacts with the fuel, mainly inside the fuel grain port, where combustion takes place. How-

ever, when a short prechamber is applied or complete vaporization of the liquid oxidizer is not satisfied, the process may likely still occur in the combustion port and, sometimes, even in the post-chamber. Then, the designed performance is impacted if the mixing and burning at a proper oxidizer to fuel ratio is not achieved inside the motor. In other words, the project of the injector system is central for the atomization and vaporization process that potentially leads to better mixing and burning with the solid fuel.

The oxidizer injection plays a crucial role in liquid and hybrid engines' combustion efficiency and performance [6]. The characteristics of the spray can significantly affect not only the efficiency but also the combustion stability [7]. Different spray characteristics can be achieved by changing the atomizer configuration. Predicting the influence of the oxidizer injector configuration on the motor characteristics such as regression rate, thrust, and specific impulse would help facilitate hybrid rocket propulsion development.

The well-designed injector may be fairly widespread in combustion efficiency in various applications such as liquid rocket propulsion systems. In general, recent well-designed injection systems have demonstrated c^* efficiencies close to 100% of the theoretical values that the

---

Nomenclature

Symbols

A_t	Throat nozzle area
A_{inj}	Area of the orifice in injector plate
C_D	Discharge coefficient
c^*_{exp}	Experimental characteristic velocity
c^*_{th}	Theoretical characteristic velocity
C_F	Thrust coefficient
D_{inj}	Diameter of orifice in injector plate
d_f	Final port diameter of the fuel grain
F	Thrust
$\bar{F}$	Average thrust
I_{sp}	Specific impulse
$\bar{G}_{ox}$	Average oxidizer mass flux
$\bar{G}_{ox\_i}$	Average initial oxidizer mass flux
g_0	Gravitational acceleration constant
L_g	Fuel grain length
$\overline{\dot{m}}$	Total average mass flow
$\overline{\dot{m}}_{ox}$	Average oxidizer mass flow rate
$\overline{\dot{m}}_f$	Average fuel mass flow rate
Δm_f	Burnt fuel mass
N_{inj}	Number of orifices in injector plate
O/F	Oxidizer-to-fuel ratio
$\overline{O/F}$	Experimental average oxidizer-to-fuel ratio
u_{ox}	Oxidizer velocity
u_z	Axial component of the oxidizer velocity
P_c	Combustion chamber pressure
$\overline{P_c}$	Average combustion chamber pressure
P_{tbt}	Test bench tank pressure of N_2O
$\bar{r}$	Average regression rate
t_b	Burning time
ρ	Density
η_{c*}	Characteristic velocity efficiency
μ	Dynamic viscosity
σ	Surface tension

Abbreviations

HRM	Hybrid rocket motor
LOX	Liquid oxygen
N_2O	Nitrous oxide
PVC	Polyvinyl-chloride
RMA	Royal Military Academy of Belgium
SH	Showerhead injector
SMD	Sauter Mean Diameter
ULB	Université Libre de Bruxelles
UnB	University of Brasilia

Subscripts

f	Fuel
inj	Injector
G	Gas
L	Liquid
ox	Oxidizer

ability to measure this parameter is the limiting factor in its determination. Examples are the Space Shuttle Main Engine (99.7%) and the upper stage XLR-132 engine (99%) [8]. However, due to the lack of maturity, the impact of the injection system on the hybrid rocket still matters of study.

The most common injector plate is the showerhead (SH) type. The SH injector sprays the oxidizer into the combustion chamber through concentric rows of orifices, and it is known to produce a high-velocity jet of oxidizer penetrating the combustion chamber. The parallel injection

Fig 1. Shelter in 1 Wing Air Base of Belgium at Beauvechain, with the hybrid motor.

ports are easy to manufacture, and the distribution and dimension of the holes determine the spray characteristics.

In this work, four different showerhead injectors were designed, manufactured, and tested to investigate the influence of the injector's configuration on motor performance. The study was performed by firing tests using 1kN lab-scale hybrid rocket motor developed at Université Libre de Bruxelles (ULB) in collaboration with the Royal Military Academy of Belgium (RMA).

2. Experimental setup and methodology

2.1. Lab-scale test bench design

All tests were carried out using the ULB-HRM test bench, installed inside a safe shelter at the 1 Wing Air Base of Belgium at Beauvechain (Fig. 1). The test stand was developed in collaboration between Université Libre de Bruxelles (ULB) and the Royal Military Academy of Belgium (RMA).

The test bench was designed for experimental investigations of a 1-kN hybrid rocket motor using liquid nitrous oxide as oxidizer and paraffin as fuel. The experimental setup consists of the motor assembled on a horizontal bench, the oxidizer feeding system, an automatic control system, and gas extraction. A data acquisition system completes the test stand subsystems framework. The test bench schematic is shown in Fig. 2.

The testing setup provides the thrust, pressures, and temperatures measurements. The thrust is measured by a load cell SENSY model 2962. The load cell had been calibrated in the range of the motor thrust employing standard weights. Another load cell (TEDEA model 615) is used to measure the weight of the oxidizer. The latter is transferred from commercial bottles to the test bench tank to provide the same conditions for each test. Both load cells are connected to a COND-SGA charge amplifier. The pressure measurements are taken on the feed line, test bench oxidizer tank, before the injector, and in the pre-chamber. Pressure transmitters used have a range of up to 100 bar. The chamber pressure is taken by a Kistler piezoelectric pressure sensor coupled with a charge amplifier type 5015. It is located in the post-combustion chamber. Type K thermocouples take temperature values plugged into a datalogger TM500.

The data acquisition system is programmed in LabView software, and it is integrated via the NI USB-6218, NI USB-9215 cards, and a control box. The LabView program allows complete remote control of the events during experiments.

The test facilities are equipped with two video cameras, GoPro 5 black, and a smartphone remotely controls them. One camera serves
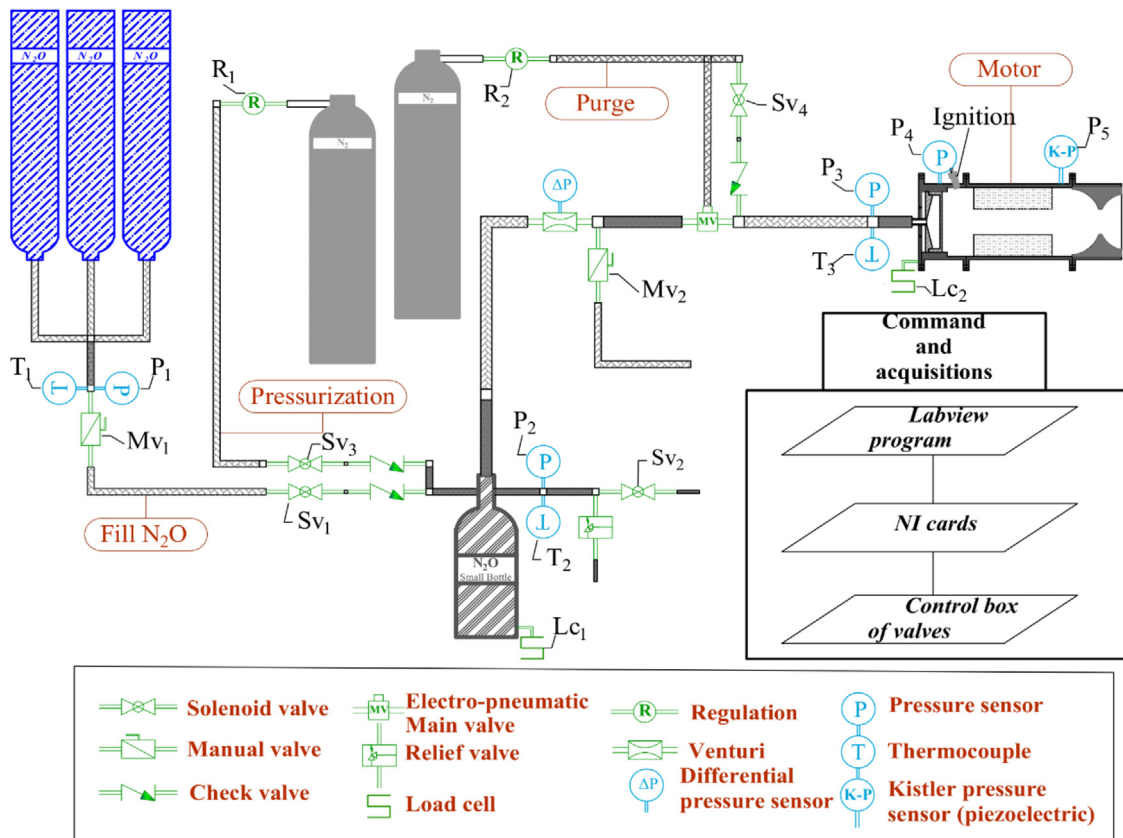
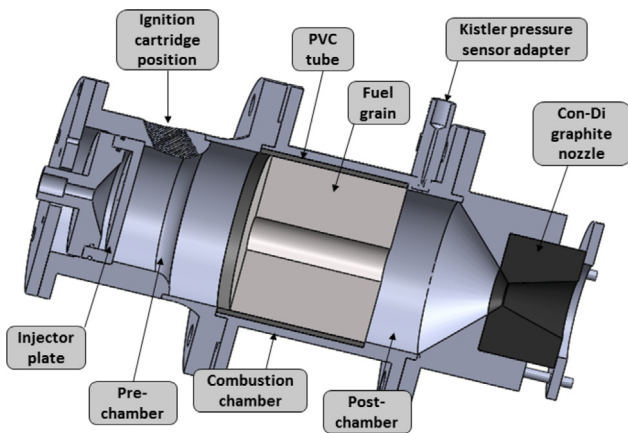**Fig 2.** Schematic of ULB-HRM test bench [10].

Fig 3. 3D view of the ULB-HRM motor.

safety purposes, and it is located in such a way that it gives the operator a global view of the experimental setup. A second camera to record the exhaust plume is placed near the nozzle. And the detailed description of the test bench, its control system, ULB-HRM motor design, ignition system, and testing procedure can be found in [9].

2.2. Motor design

The hybrid rocket motor used in this experimental investigation is shown in Fig. 3. Basically, the motor concept is modular, containing three main parts (pre-chamber, combustion chamber, and post-combustion chamber with convergent-divergent nozzle), which permits different configurations concepts as easy-to-use and easy-to-assembly.

These characteristics enable the repeatability and reliability of the experimental setup.

The pre-chamber is 100 mm long, and it is the distance between the injector plat and the front surface of the fuel grain. The ignition system and the injector adapter are placed in this section. The combustion chamber accommodates a Ø140 mm outer diameter fuel grain and a 45 mm length of post-chamber. The convergent-divergent nozzle has a graphite shell that covers the critical section and the divergent part. The throat section is Ø22 mm in diameter. After the tests, an inspection in the nozzle is done, and a new graphite insert is placed if necessary.

The total motor length is 440 mm, and the external diameter of the combustion chamber is Ø154 mm. All three parts can be disassembled in modules, which allows a fast and easy substitution of its components, mainly fuel grains, ignition cartridge charge, injector plates, and nozzle graphite insert. Table 1 represents the motor's main theoretical parameters, showing the target of 1 kN thrust for 550 g/s oxidizer mass flow rate.

2.3. Injector's design

The injection system in a classical hybrid rocket motor determines the atomization and homogeneity of the injected liquid oxidizer and the efficiency and stability of the combustion [11]. Therefore, some basic rules and requirements are followed to design the injectors used, based on Gamper and Hink, 2013 [12]. Three non-dimensional numbers can describe the atomization of the fluid injected through injector orifices. The Reynolds number, defined by Eq. 1, represents the ratio of the inertia force to the viscous force. For typical orifices, this needs to be larger than 2300 [12] to achieve turbulent flow and enhance the mixing process. The second non-dimensional number is the Ohnesorge number defined by Eq. 2. It relates viscosity to the forces of the droplet deformation. Finally, the Weber number (Eq. 3) compares the inertia

Table 1
Theoretical parameters of the ULB-HRM

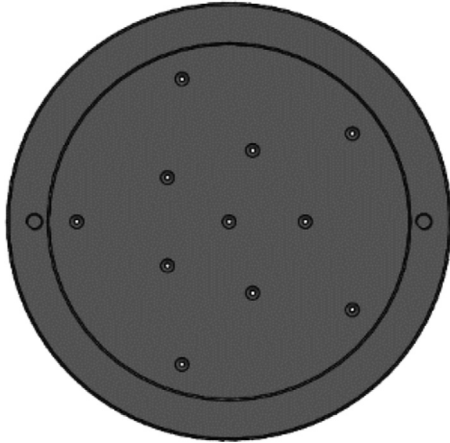| Parameter		Parameter	
Oxidizer	N_2O	O/F shift optimum	~ 7.9
Fuel	Paraffin	Oxidizer mass flow rate (g/sec)	550
Nominal thrust (kN)	1.0	Average Fuel mass flow rate (g/sec)	70
Chamber pressure (bar)	20 to 30	Total mass flow rate (g/sec)	620
Nozzle expansion rate	5.2	Operation time (s)	5 to10

Fig. 4. SH1, benchmark showerhead injector.

force to the surface forces between the liquid and gaseous phases. This number needs to be larger than 50 [12] to create small droplets.

$$Re = \frac{\rho \cdot u_{ox} \cdot D_{inj}}{\mu_L} \quad (1)$$

$$Oh = \frac{\mu_L}{\sqrt{\rho \cdot \sigma \cdot D_{inj}}} \quad (2)$$

$$We = \frac{\rho \cdot u_{ox}^2 \cdot D_{inj}}{\sigma} \quad (3)$$

Based on the theory of a plain orifice injector, the axial injection velocity (u_{ox}) is given by Eq. 4. The Sauter Mean Diameter (SMD) is the most widely used to estimate droplet size the average particle size in the atomized region. It is calculated by Eq. 5, as proposed by Tanasawa and Toyoda [13].

$$u_{ox} = \frac{\dot{m}_{ox}}{\rho_{ox} \cdot A_{inj}} \quad (4)$$

$$SMD = 47 \frac{D_{inj}}{u_{ox}} \left(\frac{\sigma}{\rho_{ox\_G}} \right)^{0.25} \left[1 + 331 \frac{\mu_L}{\left(\rho_{ox\_L} \cdot \sigma \cdot D_{inj} \right)^{0.5}} \right] \quad (5)$$

The first showerhead (SH1) has 11 orifices with a 1.4 mm diameter, which are spread equally in two different radiuses and one in the center (Fig. 4) to deliver a homogenous distribution of the oxidizer into the chamber. The injector provides around 400 g/s as the oxidizer flow rate of liquid nitrous oxide.

Fig. 5 presents the design of three other showerhead injectors (SH2, SH3, and SH4), designed based on the first results obtained using SH1. To make a fair comparison, the oxidizer mass flow rate is fixed at 550g/s for all these three injectors. The SH2 has the same configuration as SH1, but the diameter of the orifice is larger, therefore the mass flow rate is higher for an equal feeding pressure of 60 bar. The SH3 and SH4 differ by the number of orifices and their distribution density over the injector surface. Table 2 summarizes the characteristics of the N_2O injectors.

Fig. 6 compares the SMD produced using SH2, SH3, and SH4, which increases its value as the diameter of the injector orifices increases, maintaining the same oxidizer flow rate through all three injector plates. Table 3 gives some nitrous oxide properties, and the gas density is given at ambient pressure and temperature.

4. Theory and calculation

This research was performed using the same test bench as in [10] and the same method for analyzing test data. Several operational and performance parameters such as thrust, oxidizer, and fuel consumption, and pressures are collected during each test.

Pressure data are monitored at four locations: in the combustion chamber, in the test bench tank (feeding pressure), upstream and downstream the injector plate. The data acquisition sample rate is set to 8192 Hz (2^{13} Hz) to obtain signal accuracy and compare the results with another work. The sample rate also is chosen to refine the data post-processing signal. The fuel consumption is measured by weighing variation, pre- and post-test mass of the solid fuel grain.

In order to provide equal feeding pressure conditions, in all tests, the liquid N_2O is transferred from the commercial cylinders to the test facility tank and pressurized up to 60 bar by N_2 gas. A load cell is used to monitor the weight of the oxidizer test tank.

The average oxidizer mass flow rate is calculated by dividing the total injected mass of N_2O by the burning time. These data, together with the measured fuel mass flow rate, are used to evaluate the propellant total mass flow rate and the average oxidizer-to-fuel ratio $\overline{O/F}$, expressed in Eq. 6. The optimum value for a paraffin/N_2O system is reported to be near to 8.0 in a chamber pressure of 20 bar, which is high compared to other fuel/oxidizer systems in hybrid rocket propulsion. By comparison, a paraffin/LOX system is more energetic with an optimum O/F of 2.5 [14].

$$\overline{O/F} = \frac{\overline{\dot{m}}_{ox}}{\overline{\dot{m}}_f} \quad (6)$$

The average regression rate is calculated based on the experimental results and determined by the diameter variation of the fuel combustion port during the total burning time, and it is given by Eq. 7:

$$\bar{r} = \frac{d_f - d_i}{2t_b} \quad (7)$$

The definitions for the burning time and pressure rise (ignition transient time) are defined in [3]. Fig. 7 presents a typical graph of the chamber pressure during motor operation and the points where are defining the burning times. In general, the starting burning time is from 5 to 10% of the initial maximum value of pressure rise, as presented in Fig. 7, and the end of the burning time represents 20 to 40% of the initial maximum value of pressure. It varies because the combustion time, besides close, is not precisely the same for each test. In addition, these intervals from 5 to 10% for the starting burning time, or 20% to 40% for the end of burning time, are small compared to average main pressure, due to the pressure or thrust transients (ignition and termination) are quite fast in this engine.

The initial port diameter, d_i, is input data and is measured before the tests. In the first set of firing tests, the initial port diameter is equal
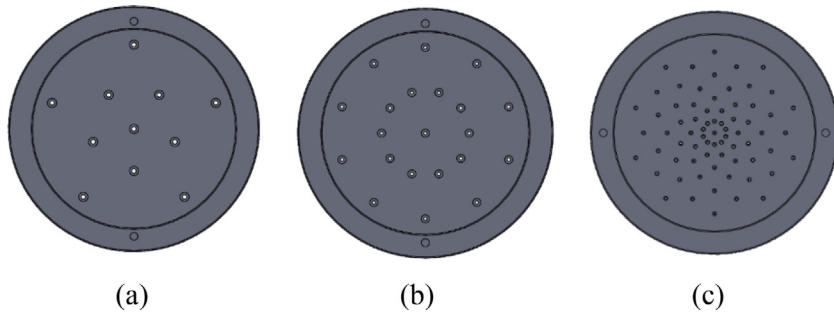
Fig. 5. Showerhead injectors design (a)-SH2, (b)-SH3, and (c)-SH4.

(a)   (b)   (c)

Table 2
Characteristics of the four SH injectors.

Injector	d_{inj}, mm	N_{inj}	u_{ox}(m/s)	Re	Oh	We	SMD (μm)
SH1	1.4	11	30.6	1.02×10^5	6.38×10^{-4}	4.22×10^3	1567.9
SH2	1.9	11	22.8	1.03×10^5	5.48×10^{-4}	3.19×10^3	2779.9
SH3	1.4	21	24.4	8.10×10^4	6.38×10^{-4}	2.67×10^3	1969.6
SH4	0.8	71	20.0	3.79×10^4	$8.44 \cdot 10^{-4}$	1.03×10^3	1450.6

Table 3
Nitrous oxide proprieties at standard state.

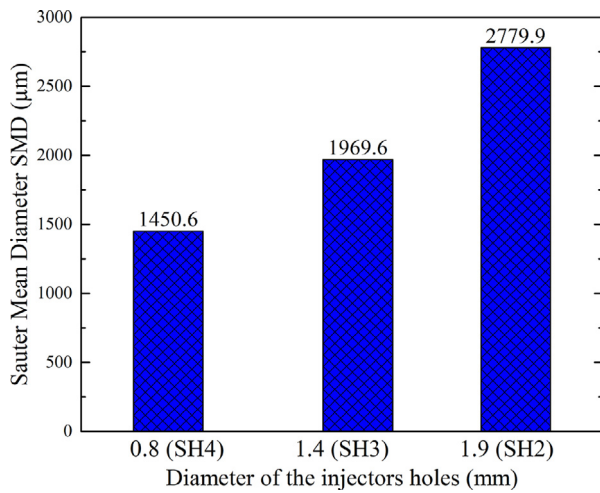| Liquid density ρ_{ox_L} (kg/m^3)	Gas density ρ_{ox_G} (kg/m^3)	Surface tension σ (N/m)	Dynamic viscosity μ_L $(Pa.s)$
772.25	1.83	0.24	325×10^{-6}

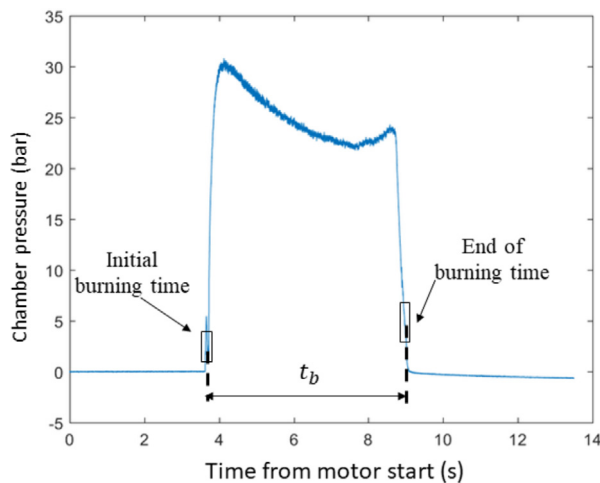**Fig 6.** SMD for different orifice diameters of the injectors.

Fig. 7. Typical chamber pressure recording trace

to 30 mm. In the second part of the work, it varies from 20 to 50 mm. The initial port diameter has a significant effect on regression rate in HRMs, as reported in Refs. [15–17] and these values are defined based and limited by combustion chamber dimensions.

The final port diameter, d_f, can not be measured directly due to a non-uniformed fuel consumption during combustion and the complicated (slightly deformed) fuel geometry after tests. In such cases, the final port diameter can be estimated by using the consumed fuel mass measurements, expressed by Eq. 8:

$$d_f = \left[d_i^2 + \frac{4\Delta m_f}{\pi \cdot \rho_f \cdot L_g} \right]^{1/2} \tag{8}$$

The oxidizer mass flux is defined as the instantaneous oxidizer mass flow rate over the cross-sectional area of the fuel grain port [3]. Its average value formula is given by Eq. 9, according to [18]. The initial value can be calculated using Eq. 10.

$$\bar{G}_{ox} = \frac{16\bar{m}_{ox}}{\pi \left(d_i + d_f \right)^2} \tag{9}$$

$$\bar{G}_{ox\_i} = \frac{4\bar{m}_{ox}}{\pi d_i^2} \tag{10}$$

The motor's thrust is measured with a load cell, which is possible because of the horizontal free sliding installation with almost frictionless linkage. From the acquired data, the average thrust $\bar{F}$ can be determined. However, the thrust is a property specific to every engine, and it is not enough to compare different rocket motors. Therefore, the specific impulse I_{sp} is used [19]. A higher number indicates better performance, i.e., the motor with the higher value of specific impulse is more efficient because it produces more thrust for the same amount of propellant. The specific impulse is calculated based on Eq. 11:

$$I_{sp} = \frac{\bar{F}}{\bar{m} \cdot g_0} \tag{11}$$

The theoretical I_{sp} represents the ideal performance of the motor and can be achieved at a certain O/F. It is calculated for different chamber pressures with the Explo5 software [20], as shown in Fig. 8.

The characteristic velocity c^* is a ballistic parameter that quantifies motor performance, and it can be used to compare different propellants
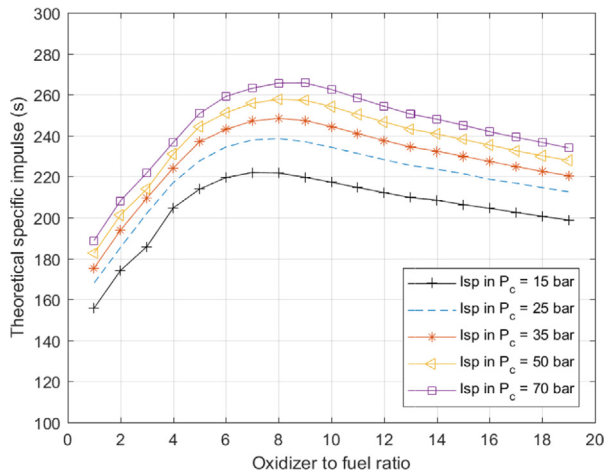
Fig. 8. Determination of the theoretical I_{sp} as a function of O/F for different conditions of chamber pressure.
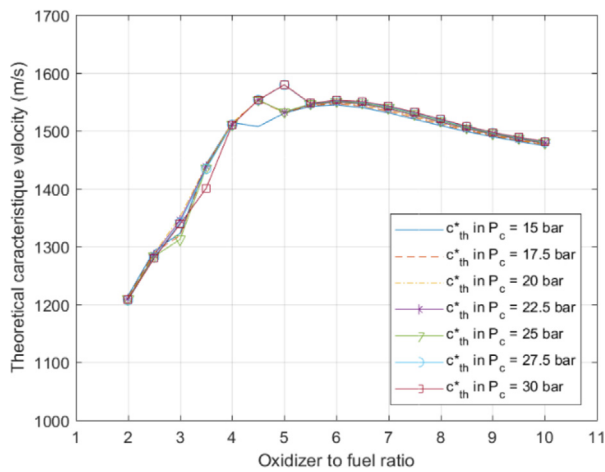

Fig. 9. Determination of the theoretical c_{th}^* as a function of O/F for different conditions of chamber pressure

Fig. 10. Characteristic velocity graph showing the calculation method of the motor efficiencies.

with the following recording setting: 120 fps speed and 1080 dpi resolution. An "intensity factor" is defined to illustrate and to characterize the different appearances of the recorded exhaust plume:

"2" for a large explosion flame as shown in Fig. 11-a,
"1" for stable flame combustion as shown in Fig. 11-b,
"0.5" for rather stables flames as shown in Fig. 11-c, and
"0" for flame blow-out and low-intensity flame as shown in Fig. 11-d.

The influence of the ignition cartridge combustion on the main performance characteristics was also evaluated. It is concluded that the ignition cartridge contribution to the thrust is negligible because the fuel mass consumed during the ignition phase is lower than 15 grams, which represents less than 1.2% of the total fuel mass [9].

5. Accuracy and reproductivity of firing test

The used instrumentations exhibit a small systematic error, and, consequently, high accuracy of the test results may be achieved. Nevertheless, the overall reproductivity of the firing test has a more significant error compared to the accuracy of the used sensors used and their instrumental error. All sensors are calibrated periodically before a test campaign. Many working parameters, all along with the experimental setup, present a form of non-fully controllable output or non-fully controllable variables:

- Ignition of the starter composition;
- Turbulence in the igniting gases;
- Ignition of the paraffin fuel surface;
- Quality (shape, density, etc.) of the fuel surface;
- Quality of the combustion, achievement of chemical equilibrium, the unburnt mass of fuel;
- Turbulence inside the combustion chamber;
- Combustion instability;
- And some other environmental factors.

All these parameters will somehow affect the final reproductivity of the results. To minimize the impact of these uncertainties on the quality of the experimental data, the tests are repeated at least 3 (three) times, using the same inlet conditions, to ensure the reliability of the results. Basic statistics performed on shows a fluctuation from 1% to 5% of the average values.

combinations [3]. The experimental c_{exp}^* is given by Eq. 12. The combustion efficiency of the motor is given by Eq. 13 and it is the ratio of the measured characteristic velocity, calculated by Eq. 12, and theoretical characteristic velocity calculated with the EXPLO5 thermochemical software [20]. The c_{th}^* is calculated for each test because different injectors and conditions give a variation in the chamber pressure and the O/F ratio. The data to estimate c_{th}^* is generated with the Explo5 software [20] and can be visualized in Fig. 9.

$$c_{exp}^* = \frac{\overline{P_c \cdot A_t}}{\overline{\dot{m}}} \quad (12)$$

$$\eta_{c^*} = \frac{c_{exp}^*}{c_{th}^*} \quad (13)$$

In the data analysis, the combustion efficiency (η_{c*}) is calculated applying Eq. 13, with a c_{th}^* corresponding to $\overline{O/F}$ data. This efficiency represents a realistic estimation of the motor performance because it uses a measured average oxidizer-to-fuel ratio. In Fig. 10, the theoretical characteristic velocity at 17.5 bar combustion chamber pressure is presented. A red rhombus represents the experimental characteristic velocity value, and the thrust coefficient is defined by Eq. 14 [3].

$$C_F = \frac{F}{P_c \cdot A_t} \quad (14)$$

The exhaust plume is the only visually available property of combustion. To investigate it, each firing test was recorded using a video camera
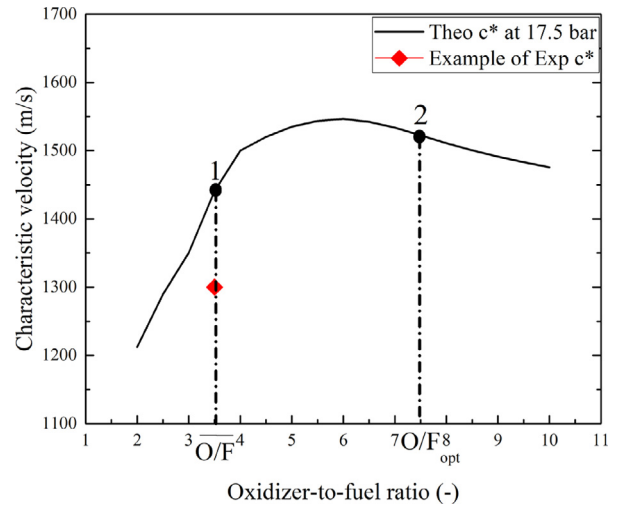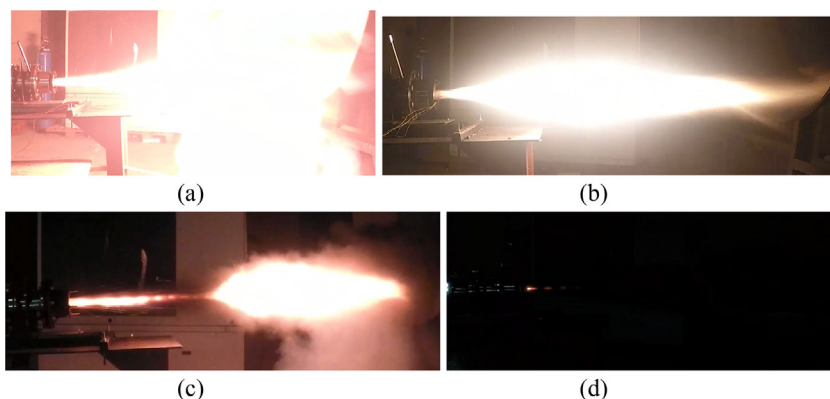
Fig 11. Exhaust plumes are characterized by an intensity factor with values of: a- "2", b- "1", c- "0.5", and d- "0".

Table 4
Test results obtained with SH1 injector (average values).

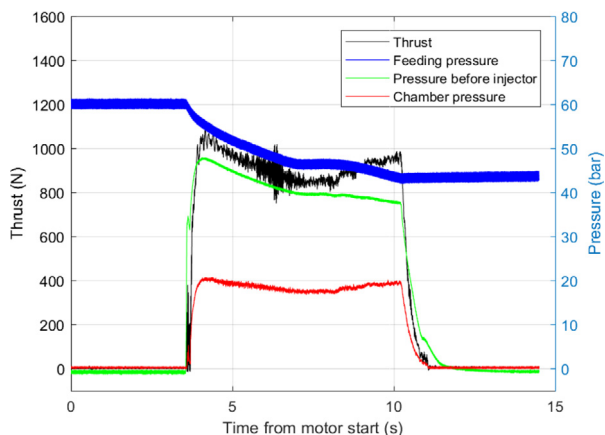| Test n°	P_{tbt}, bar	d_i, mm	$\overline{\dot{m}}_{ox}, g/s$	t_b, s	d_f, mm	$\bar{G}_{ox\_i}, g/cm^2 s$	$\bar{G}_{ox}, g/cm^2 s$	$\overline{O/F}$	$\bar{r}, mm/s$	I_{sp}, s	P_c, bar	C_F	$\eta_{c^*}, \%$ at$\overline{O/F}$
SH1-1	60.0	30.0	393.8	6.8	124.4	55.7	8.4	2.7	6.90	162.9	17.7	1.29	95.3
SH1-2	60.0	30.0	393.3	6.5	121.0	55.6	8.8	2.5	7.01	168.9	18.2	1.31	97.8
SH1-3	60.0	30.0	387.7	6.4	118.6	54.9	8.9	2.6	6.96	165.6	17.3	1.31	95.0

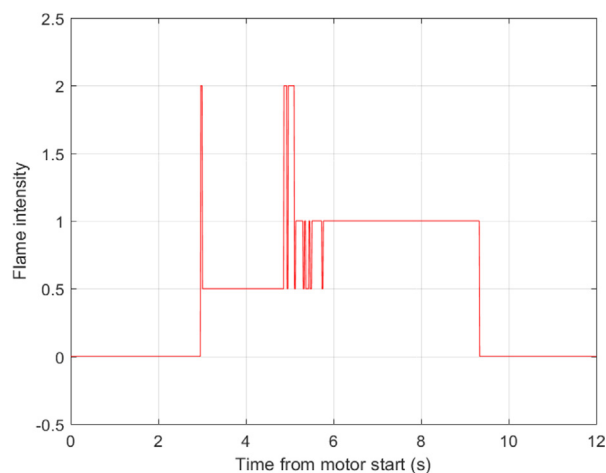**Fig. 12.** Thrust and pressures as a function of time, test #SH1-3.

Fig. 13. The intensity value of the exhaust plume of firing test #SH1-3.

6. Experimental results

The firing tests were conducted at the 1 Wing Air Base of Belgium located in Beauvechain. No major problems occurred during these campaigns, except for a few tests where the mass of the N$_2$O tank or thrust was not correctly recorded. These tests have not been post-processed and presented.

6.1. SH1 firing test results

The first test series were performed with the injector SH1. This injector has an average oxidizer mass flow rate of 391.6 g/s, and its geometry is shown in Fig. 4. Table 4 reports the average performance obtained with this injector. Initial conditions such as injection pressure (or pressure in the oxidizer tank), grain length, and grain fuel composition were kept unaltered.

A typical graph of the generated thrust and the three pressure (feeding pressure, pressure before injector, and chamber pressure) are presented in Fig. 12. The average experimental specific impulse was around 80% of the theoretical value and average oxidizer to fuel rate $\overline{O/F}$ represents 35% of the theoretical maximum value.

Fig. 13 represents the evolution of the flame intensity generated by the motor during test #SH1-3. Two peaks are noticeable. They represent an explosive combustion (hard ignition) in the plume. The oxidizer injection at low temperature causes the first peaks; hence a blow-out occurs, and the flame falls back downstream of the injector. Meanwhile, heat transfer to the fuel grain surface keeps on and produces more fuel vapor, which, when mixed appropriately with the injected oxidizer, causes a second peak. Flame blow-out can occur due to the mixture ratio variations, as cited in Refs [21, 22]. Generally, one observes a strong flame blow-out during the first half of the combustion, i.e., between 5 to 5.8 s. The backflow is what we observe in the trace in Fig. 13, after the second explosion. The high axial velocity produced by the SH1 configuration propels the gaseous oxidizer through the nozzle, reducing the combustion chamber's residence time, preventing appropriate mixing with the evaporating fuel, and eventually exiting the motor without proper reaction/combustion.

Because of the low value of oxidizer to fuel ratio reached with this injector SH1 and the phenomenon of blow-out observed during all tests with SH1, we propose the three following injectors SH2, SH3, and SH4 (Fig. 5). These injectors made it possible to increase the oxidizer mass

Table 5

Test results obtained with SH2, SH3, and SH4 injectors (average values).

Test n°	P_{tbt}, bar	d_i, mm	t_b, s	$\bar{\bar{m}}_{ox}, g/s$	d_f, mm	$\bar{G}_{ox\_i}, g/cm^2s$	$\bar{G}_{ox}, g/cm^2s$	$\overline{O/F}$	$\bar{r}, mm/s$	I_{sp}, s	P_c, bar	C_F	$\eta_c, \%$ at $\overline{O/F}$
SH2-1	60.0	30.0	5.3	529.2	105.6	74.9	14.7	3.6	7.18	172.2	24.1	1.25	90.1
SH2-2	60.0	30.0	5.2	542.5	107.4	76.7	14.6	3.6	7.28	165.2	24.4	1.18	87.5
SH2-3	60.0	30.0	5.3	528.9	107.8	74.8	14.2	3.4	7.41	170.5	23.1	1.23	89.2
SH3-1	60.0	30.0	5.3	538.3	105.5	76.2	14.9	3.5	7.33	162.0	22.8	1.27	89.2
SH3-2	60.0	30.0	5.2	543.2	105.5	76.8	15.1	3.6	7.22	171.5	23.8	1.29	89.8
SH3-3	60.0	30.0	5.3	537.6	107.8	76.1	14.4	3.5	7.38	172.3	24.4	1.28	93.3
SH4-4	60.0	30.0	5.1	550.0	108.3	77.8	14.6	3.5	7.70	169.0	24.1	1.27	90.4
SH4-5	60.0	30.0	5.2	537.5	109.4	76.0	14.1	3.5	7.69	166.8	23.3	1.28	92.5
SH4-6	60.0	30.0	5.1	544.5	107.8	77.0	14.6	3.5	7.61	165.6	24.3	1.30	93.4
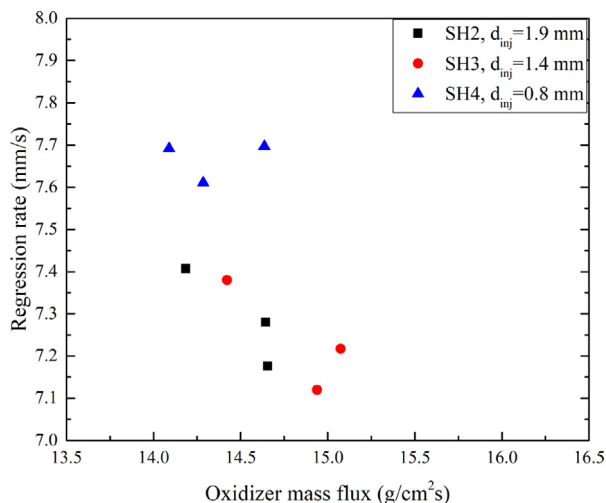
Fig. 14. Regression rate in function of the average oxidizer mass flux for the different showerhead injectors

Fig. 16. Comparison of the specific impulse, $\overline{O/F}$ and the HRM efficiencies for different SH injectors.

flow rate to reach the theoretical value of 550 g/s and to study the impact of different dimensions of the injector orifices.

6.2. Firing test results of SH2, SH3, and SH4

After the benchmark injector tests (SH1), two sets of firing tests are carried out. At first (section 6.2.2), the influence of the showerhead injector geometry, as number and size of elements (holes), and its impacts on the overall performance of hybrid rocket combustion were investigated. In the second part (section 6.3), the fuel grain initial port effect is studied using SH4. Table 5 presents the motor operations conditions and the performance parameters depending on the injectors type. The following sections discuss these tests' results and all initial conditions (injection pressure, initial port of fuel grain, grain length, grain composition) that were kept the same through all tests.
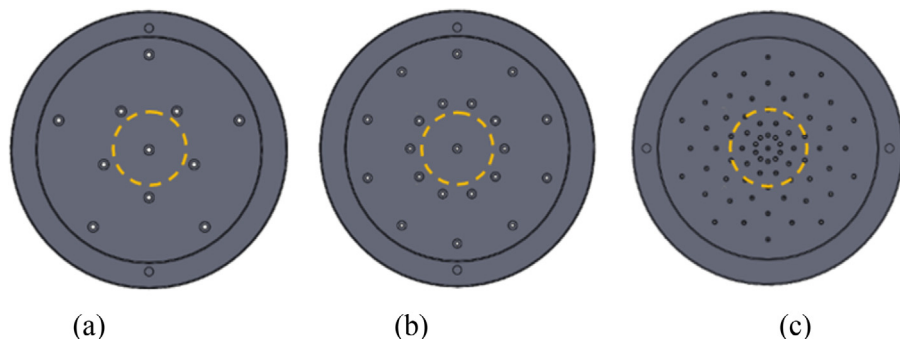
6.2.1. Oxidizer Mass flow rate and discharge coefficient

One of the main investigated parameters was the oxidizer mass flow rate to confirm whether the design target value of 550 g/s was obtained. The importance of this variable lies in the fact that a fair comparison between the three injectors is possible when similar conditions are achieved. Taking into consideration the test results, the average oxidizer mass flow rate $\bar{m}_{ox}$ of 533.5 g/s, 539.7 g/s, and 544 g/s were obtained for the injectors SH2, SH3, and SH4, respectively, right near the designed values. The real discharge coefficient was calculated to be 0.32, which is close to the assumed of 0.33, and that was based on previous experimental results of the SH1 injector [9].

6.2.2. Influence of orifice size

The influence of injection elements orifice dimensions on the regression is presented in Fig. 14. SH4 has the highest regression rate for the

Fig. 15. Representation of injector holes distribution vis-a-vis initial port grain diameter: (a)-SH2, (b)-SH3 and (c)-SH4

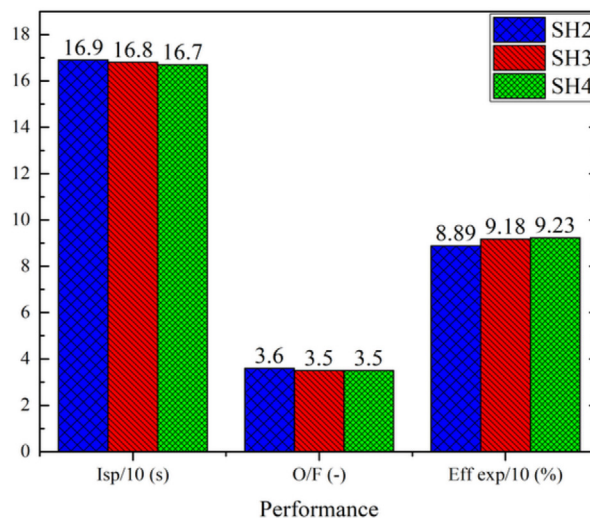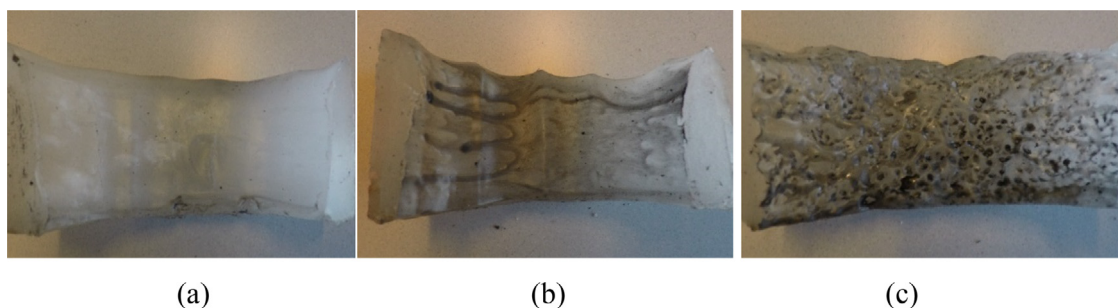**Fig. 17.** Illustration of the grain interior after combustion for fuel grains with (a)-SH2, (b)-SH3, and (c)-SH4
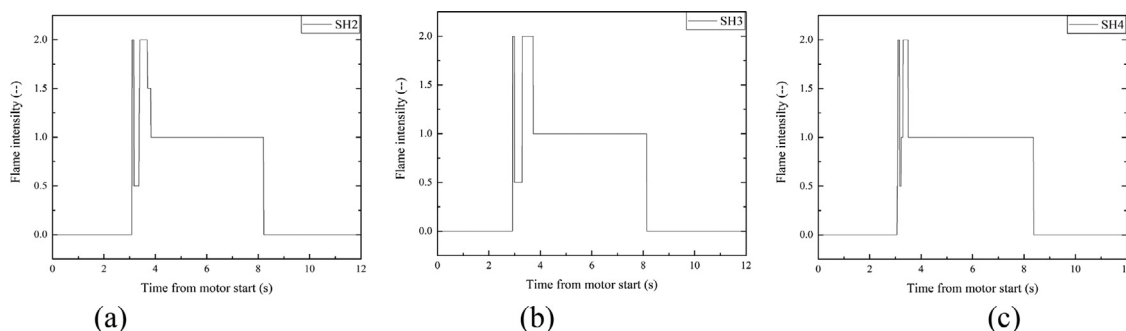

Fig. 18. The intensity value of the exhaust plume for firing tests with injectors: (a)- SH2, (b)-SH3 and (c)-SH4

same average oxidizer mass flux and initial fuel port. An increase of 5 % is achieved compared to SH2 and SH3. This implies that for an equal $\bar{G}_{ox}$, the injector with better spray pattern due to the number of the elements has the highest regression rate. We assume this can partly be attributed to the increase in turbulence and the smallest droplets generated with the SH4 injector. That allows a better distribution of the oxidizer, maximizing the atomization process and improving the mixture with the vaporized fuel grain. In the configuration presented in Fig. 15, initially, for the injector SH4 and the fuel grain with a port diameter d_i= Ø30 mm, more oxidizer droplets were injected directly in the fuel port compared to SH2 and SH3 at the same conditions. Between the SH2 and SH3 injectors, as presented in Fig. 16, there is no significant difference in the motor's overall performance. SH4 exhibits higher c^*efficiency (η_{c*}), and C_F, and the I_{sp} equivalent to the other injectors.

Based on the different performances of the injectors, we presume that some amount of fuel is just ejected out of the motor without participating in the combustion process. This is likely the case of the SH2, which has larger orifice elements, generating a jet with larger droplets (SMD number), giving less surface per volume to react and decreasing the combustion efficiency η_{c*} [13].

After combustion, the fuel grains used with SH2 and SH3 injectors exhibit longitudinal channels, and their burning surfaces are smooth (Fig. 17 - a & b). The grain when SH3 is used (Fig. 17 - b) has more channels than SH2 (Fig. 17 - a) because of the number of injector elements in SH3 increases. The grain tested with SH4 has various craters (small pits) due to the distribution and the number of injector elements (orifices), likely because of the turbulence generated, which helps the increase of the regression rate (Fig. 14).

When investigating the exhaust flame stability, as presented in Fig. 18, it was observed that the flame is much more stable in the firings with SH2, SH3, and SH4 compared to SH1 (Fig. 13) due to the nonappearance of the blow-out. The last injector, SH4, exhibits the most stable exhaust flame, which can be seen in the flame intensity recorded (Fig. 18), where the time gap between the two peaks is smaller in Fig. 18-c than Fig 18-b and 19-c. The plume after 2 seconds and 3 seconds for typical firing tests with SH2, SH3, and SH4 are in Fig. 19. Based on that, it is possible to note that the shape of the ex-

Table 6
Initial percentage of $\bar{m}_{ox}$ through different d_i.

, mm	Initial percentage of $\overline{m}_{ox}$ through d_i
20.0	23 %
30.0	37 %
40.0	51 %
50.0	65 %

haust plumes is slightly influenced by the size and distribution of the orifices.

After a comparison between the three injectors, we found that the injector SH4 exhibits better performance with a 5% increase in regression rate and a higher c^* efficiency (η_{c*}). The best signal of exhaust flame intensity is also observed with SH4. Due to these advantages, SH4 was chosen to carry out the next part of the firing tests to study the effect of the fuel grain initial port.

6.3. Influence of the initial fuel grain port diameter

A series of firing tests were performed using the SH4 injector to investigate the influence of the initial fuel port diameter over the motor performance. This study has a dual purpose. First, it is required to have different values of the oxidizer mass flux to obtain a regression rate law for this specific propellant combination. The second reason is to understand the influence of the oxidizer flow related to the fuel grain geometry.

All initial conditions (injection pressure, grain length, grain fuel composition) were kept constant, as in previous test sets, except the initial fuel grain port diameter, to analyze $\bar{G}_{ox}$ influence. Four different fuel grains with varying initial port diameters were tested. The port diameters are, respectively, 20, 30, 40, and 50 mm. By reducing the initial port diameter, both $\bar{G}_{ox\_i}$ and $\bar{G}_{ox}$ are consequently increased.

Figure 20 illustrates the initial fuel combustion port position related to the SH4 injector plate, and Table 6 shows the percentage of oxidizer injected directly into the fuel grain for each initial condition. The in-
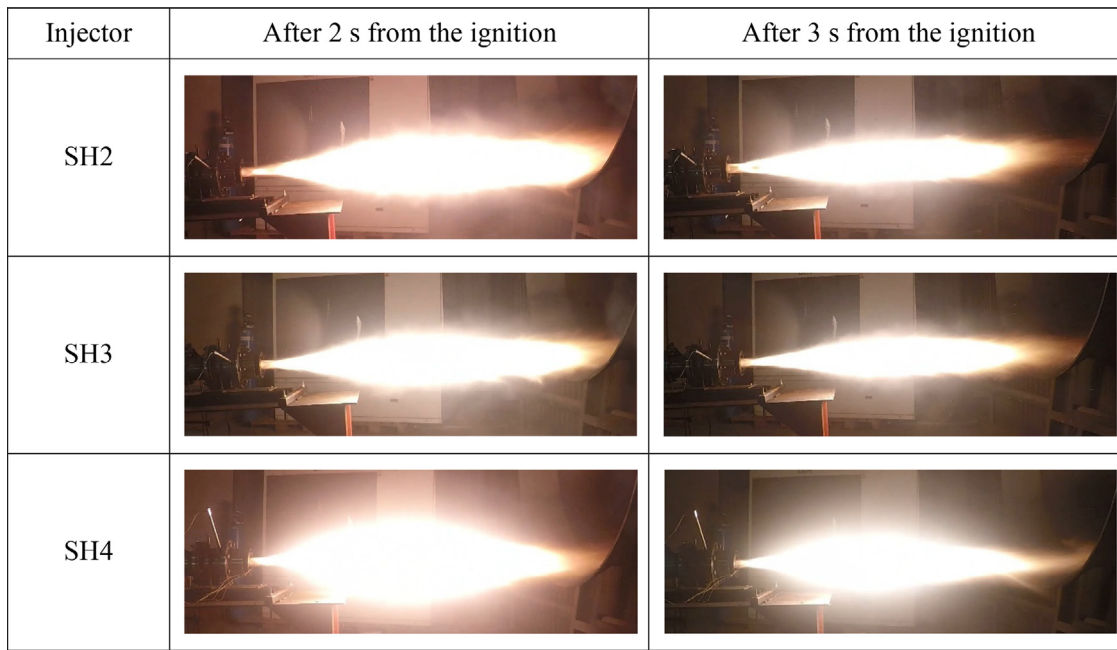
Injector	After 2 s from the ignition	After 3 s from the ignition
SH2		
SH3		
SH4		

Fig. 19. Typical exhaust flame after 2 and 3 seconds from the ignition with the different injectors.

Table 7
Test results obtained with SH4 injector with a different initial port diameter of the fuel grain (average values).

Test n°	P_{tbt}, bar	d_i, mm	t_b, s	$\overline{\dot{m}}_{ox}$, g/s	d_f, mm	$\bar{G}_{ox\_i}$, g/cm²s	$\bar{G}_{ox}$, g/cm²s	$\overline{O/F}$	$\bar{r}$, mm/s	I_{sp}, s	P_c, bar	C_F	η_{c^*}, % at $\overline{O/F}$
SH4-1	60.0	20.0	5.2	551.3	109.5	175.5	16.7	3.4	8.66	163.5	24.8	1.22	92.9
SH4-2	60.0	20.0	5.1	549.8	111.3	175.0	16.2	3.3	8.96	150.2	25.1	1.11	95.9
SH4-3	60.0	20.0	5.2	553.6	109.8	176.2	16.7	3.4	8.72	151.9	25.4	1.10	95.2
SH4-4	60.0	30.0	5.1	550.0	108.3	77.8	14.6	3.5	7.70	161.7	24.1	1.22	90.4
SH4-5	60.0	30.0	5.2	537.5	109.4	76.0	14.1	3.5	7.69	160.9	23.3	1.23	89.0
SH4-6	60.0	30.0	5.1	544.5	107.8	77.0	14.6	3.5	7.61	165.6	24.3	1.23	92.3
SH4-7	60.0	40.0	5.1	537.7	112.2	42.8	11.8	3.5	7.15	169.9	23.2	1.31	88.7
SH4-8	60.0	40.0	5.1	543.2	111.9	43.2	12.0	3.4	7.02	164.4	23.3	1.28	89.0
SH4-9	60.0	40.0	5.1	537.5	109.5	42.8	12.2	3.6	6.88	158.9	23.3	1.21	89.0
SH4-10	60.0	50.0	5.2	547.8	113.2	27.9	10.5	3.7	6.04	164.1	22.7	1.29	85.1
SH4-11	60.0	50.0	5.1	548.0	112.1	27.9	10.6	3.8	6.08	167.7	24.2	1.24	89.7
SH4-12	60.0	50.0	5.1	544.1	110.9	27.7	10.7	4.0	5.93	168.8	23.8	1.25	88.2
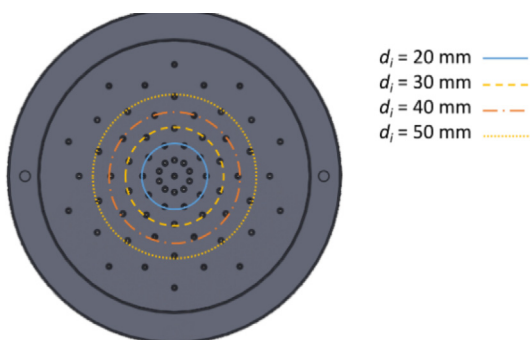
Fig. 20. Illustration of the interior diameter of the fuel grain compared to the injector plate orifices.

d_i = 20 mm ——
d_i = 30 mm – – –
d_i = 40 mm – · –
d_i = 50 mm ·······

Table 8
Performance parameters for fuel grains with different initial port diameters (average values).

, mm	$\bar{r}$, mm/s	$\overline{O/F}$	$\bar{I}_{sp}$, s	η_{c^*}, % at $\overline{O/F}$
20.0	8.78	3.4	155.2	94.6
30.0	7.67	3.5	162.8	90.6
40.0	7.02	3.5	164.4	88.9
50.0	6.02	3.8	166.9	87.7

tion [12]. Table 7 presents the experimental results for this set of firing tests.

After test sets, all fuel grains were studied to investigate their overall conditions. The grain with an initial port diameter of 20 mm has small craters, while the one of 50 mm is much smoother (Fig. 21). The gain in smoothness is coherent with the increase in initial fuel port diameter. We assume that turbulent flows are created when the oxidizer flow is not injected directly through the port. This extra-turbulent flow is subsequently guided through the fuel port due to the pressure difference between the chamber pressure and the atmosphere (exit of the nozzle). When passing through the fuel port, the turbulent flow may cause these cavities.

When investigating the influence on the performance parameters (Table 8 and Fig. 22), a change in the initial fuel port diameter increases
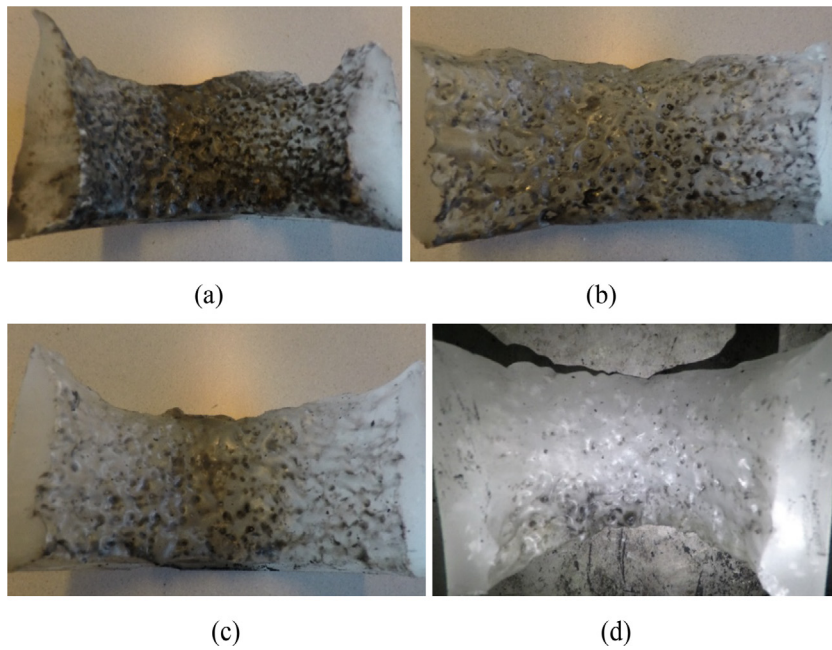
jector elements arrangement is essential to obtain homogeneous combustion [12], once that the combustion port changes during the time, causing an O/F shift, and it can impact the motor performance. A grain with a d_i of 20 mm, initially, only admits 23% of the nitrous oxide flow through the fuel port, whereas 50 mm d_i allows 65%.

In order to have a uniform homogeneous distribution of the liquid oxidizer, the injector orifices may be arranged according to the shape of the solid fuel port. It is required for homogeneous combus-

Fig. 21. Illustration of the grain interior after combustion for fuel grains with different initial diameters (mm): (a)-20, (b)-30, (c)-40, and (d)-50
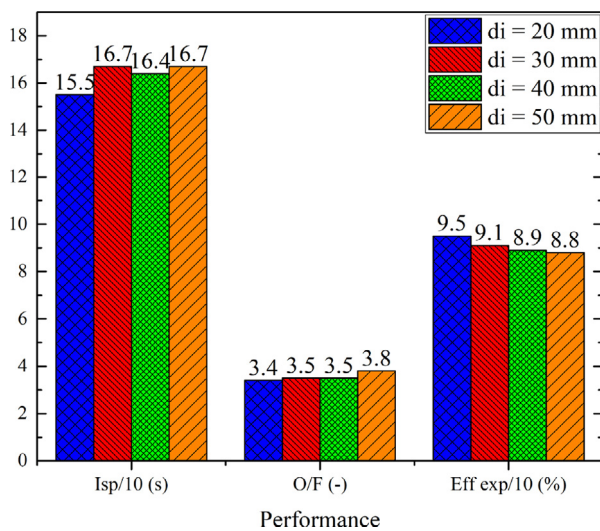

Fig. 22. Comparison of specific impulse (s), $\overline{O/F}$ and efficiencies (%) between different grain size diameters.

Fig. 23. Regression rate variation with initial port of fuel grain.

the thrust generated by the specific impulse's growth. The smallest diameter port grain (20 mm) causes the lowest average specific impulse, coherent with the theory and experimental results presented in [23]. Karabeyoglu et al. (2012) also stated that the specific impulse increases with increasing port grain diameter due to a faster change in the geometrical area [24]. The average efficiencies in optimal O/F are close to each other for all diameters tested. This, in combination with the highest value for $\overline{O/F}$ for the 50 mm diameter fuel port grain, gives the lowest average efficiency at an $\overline{O/F}$ value of 87.7 %. This is due to a lower c^* (Eq. 13) in combination with a higher c_{th}^* (Fig. 10).

Fig. 23.

When the average value over all tests is taken, a gain in regression rate with decreasing initial port diameter of the fuel grain is noticed. An increase in average port diameter for the same oxidizer mass flux will also reduce the regression rate, and it was also reported by Swami & Gany [25]. The fuel port size is an important design pa-
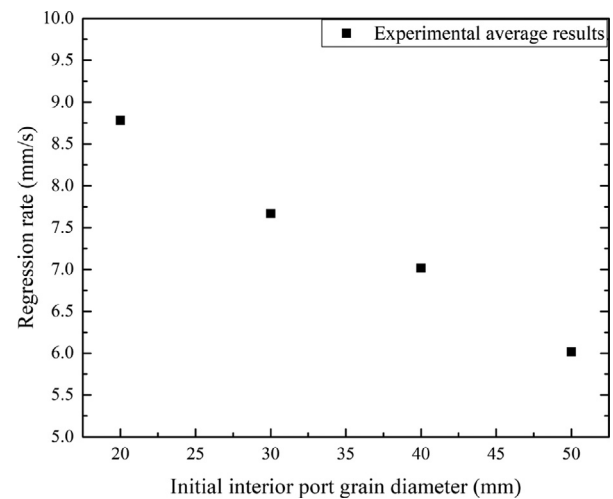
rameter to determine the fuel surface regression rate in hybrid rockets [16].

For hybrid propulsion, the fuel regression rate is assumed to be governed by the oxidizer mass flux, and it can be expressed as follows (Eq. 15), as the regression rate law:

$$\bar{r} = a \, G_{0x}^n \tag{15}$$

The port diameter length ratio (D/L) of the fuel grain is also increasing (smaller initial diameter for the same initial length), and this is known to give higher regression rates [23]. Fuel regression rate law is applied to fit the experimental result, which is presented in Fig. 24. The parameters a and n mentioned in Eq. 16, were obtained by interpolation analysis. Unit used for regression rate is mm/s and for oxidizer mass flux is g/cm²s. The calculated n exponent (0.78) is coherent with published theoretical values [24].

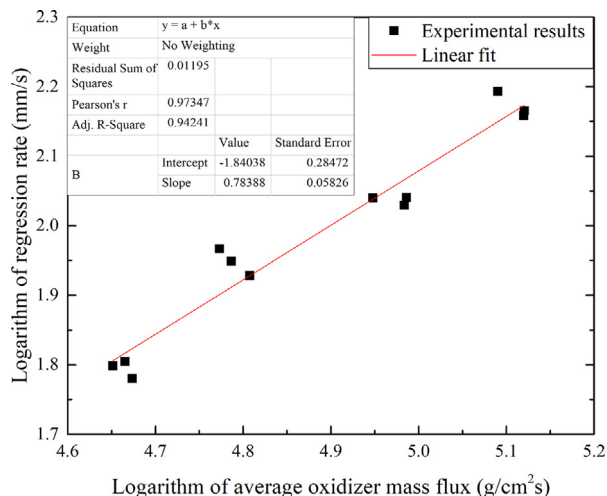$$\bar{r} = 0.159 \, G_{0x}^{0.78} \tag{16}$$

Fig. 24. Regression rate law

7. Conclusions

This paper presents a series of firing tests with different showerhead (SH) injector configurations, named SH1, SH2, SH3, and SH4. In the first part, the effect of showerhead injector configurations on the overall performance of hybrid rocket combustion is analyzed. The designs differ by the orifice's distribution, number, and size of elements. In the second part, the effect of the initial port of the fuel grain was studied, and the regression rate coefficients were determined for this specific propellant combination.

Since hybrid rocket motors are not extensively studied as liquid and solid propulsion systems, this work aims to improve the technical literature with experimental data of N_2O/paraffin fuel, focusing on the influence of a specific injector design over motor performance. Because it is one of the most common types of injector plate, the showerhead injector was chosen to examine the impact of the liquid oxidizer pattern on the operation of a hybrid rocket motor. The injector also was selected because it allows comparing the results with other experimental and theoretical research.

To study the influence of the injector elements (oxidizer channels diameter), three injectors were compared: SH2, SH3, and SH4 with injector element diameters of 1.9 mm, 1.4 mm, and 0.8 mm, respectively. The injector with the smallest orifice size (SH4) gives an increase of 5 % on the solid fuel regression rate (~7.7 mm/s) and higher c^* efficiency (η_{c*}). Concomitant, both SH2 and SH3 present similar values of average regression rates, i.e., 7.3 mm/s, and equivalent specific impulse.

However, the injector design influences another critical parameter, the flame blow-out phenomenon. It was observed that flame blow-out tends to disappear when SH1 is not used, mainly by increasing the oxidizer mass flow rate from around 400 g/s to 550 g/s, with SH2, SH3, and SH4. Consequently, the oxidizer to fuel ratio increased from 2.5 to 3.5. SH4 produces the most stable flame with the highest number of injectors orifice and the finest oxidizer spray with the smallest SMD. And it permits us to conclude that the exhaust plume and the blow-out phenomena are directly linked with the injector orifice distribution and the oxidizer-to-fuel ratio.

The design of the injector must be fully adapted to the fuel grain geometry, and in the ideal case, the oxidizer is injected directly into the fuel grain port. This improves the combustion homogeneity, resulting in a more stable thrust profile and increasing the specific impulse, as shown in Table 7.

The combustion efficiency is sometimes lower for hybrid rocket motors than for liquid or solid systems, and if adequate mixing is not allowed, c^* efficiency can drop below 0.9 [26]. In this research, for the

injector SH4, it was obtained values from 0.85 to 0.95, depending on $\bar{G}_{ox}$. Considering that in hybrid rocket engines, the O/F shift varies with burning time, the design of the injector helps increase the overall motor efficiency.

Another result delivered by the experimental data is the regression rate law (Eq. 16) for N_2O/paraffin-based fuels. The regression rate law is a piece of essential information for future updates in the ULB motor design. In parallel, it can be noticed in the hybrid literature that even with various experimental works using nitrous oxide and paraffin, there are not many studies that present the fuel regression rate law because of the number of tests necessary to obtain this parameter. For these specific motor and propellant configurations, the regression rate law is $\bar{r} = 0.159 G_{ox}^{0.78}$. The mass-flux exponent n (0.78) is coherent with published theoretical values [24].

Declaration of Competing Interest

The authors declare that they have no known competing financial interests or personal relationships that could have appeared to influence the work reported in this paper.

References

[1] M. Invigorito, G. Elia, M. Panelli, Numerical modeling of self-pressurizing oxidizers for hybrid rocket injection, 2015 EUCASS, 2015.

[2] D. Altman, A. Holzman, Overview and history of hybrid rocket propulsion, Prog. Astronaut. Aeronaut. 218 (2007) 1.

[3] G.P. Sutton, O. Biblarz, Rocket Propulsion Elements, John Wiley & Sons, 2016.

[4] G. Cai, C. Li, S. Zhao, H. Tian, Transient analysis on ignition process of catalytic hybrid rocket motor, Aerosp. Sci. Technol. 67 (2017) 366–377.

[5] C. Carmicino, F. Scaramuzzino, A.R. Sorge, Trade-off between paraffin-based and aluminium-loaded HTPB fuels to improve performance of hybrid rocket fed with N2O, Aerosp. Sci. Technol. 37 (2014) 81–92.

[6] C. Carmicino, A.R. Sorge, Performance comparison between two different injector configurations in a hybrid rocket, Aerosp. Sci. Technol. 11 (1) (2007) 61–67.

[7] C. Carmicino, A.R. Sorge, Role of injection in hybrid rockets regression rate behaviour, J. Propul. Power 21 (4) (2005) 606–612.

[8] D.H. Huang, D.K. Huzel, Modern Engineering for Design of Liquid-Propellant Rocket Engines, American Institute of Aeronautics and Astronautics, 1992.

[9] M. Bouziane, A.E. De Morais Bertoldi, P. Milova, P. Hendrick, M. Lefebvre, Development and Testing of a Lab-scale Test-bench for Hybrid Rocket Engines, in: 2018 SpaceOps Conf., 2018, p. 2722.

[10] M. Bouziane, A.E.M. Bertoldi, P. Milova, P. Hendrick, M. Lefebvre, Performance comparison of oxidizer injectors in a 1-kN paraffin-fueled hybrid rocket motor, Aerosp. Sci. Technol. 89 (2019) 392–406.

[11] G. Elia, M. Invigorito, M. Di Clemente, R. Votta, G. Ranuzzi, Injection system design of an N2O-paraffin hybrid rocket demonstrator, Young International Conference, 2015.

[12] E. Gamper, R. Hink, Design and Test of Nitrous Oxide Injectors for a Hybrid Rocket Engine, Deutsche Gesellschaft für Luft-und Raumfahrt-Lilienthal-Oberth eV, 2013.

[13] A.H. Lefebvre, V.G. McDonell, Atomization and Sprays, CRC press, 2017.

[14] M.J. Chiaverini, K.K. Kuo, Fundamentals of Hybrid Rocket Combustion and Propulsion, American Institute of Aeronautics and Astronautics, 2007.

[15] D. Bianchi, F. Nasuti, C. Carmicino, Hybrid rockets with axial injector: port diameter effect on fuel regression rate, J. Propul. Power 32 (1) (2016) 984–996.

[16] G. Cai, P. Zeng, X. Li, H. Tian, N. Yu, Scale effect of fuel regression rate in hybrid rocket motor, Aerosp. Sci. Technol. 24 (1) (2013) 141–146.

[17] D.R. Greatrix, Regression rate estimation for standard-flow hybrid rocket engines, Aerosp. Sci. Technol. 13 (7) (2009) 358–363.

[18] A. Karabeyoglu, G. Zilliac, B.J. Cantwell, S. DeZilwa, P. Castellucci, Scale-up tests of high regression rate paraffin-based hybrid rocket fuels, J. Propul. Power 20 (6) (2004) 1037–1045.

[19] N. Hall, Specific Impulse, 2015 Retrieved from https://www.grc.nasa.gov/WWW/K-12/airplane/specimp.htmlr (accesed 23-04-2019).

[20] "EXPLO5, Retrieved from http://www.ozm.cz/en/explo-5-software/, (accesed 23-07- 2018)."

[21] T. Boardman, D. Brinton, R. Carpenter, T. Zoladz, An experimental investigation of pressure oscillations and their suppression in subscale hybrid rocket motors, in: 31st Joint Propulsion Conference and Exhibit, 1995, p. 2689.

[22] J. Pucci, The effects of swirl injector design on hybrid flame-holding combustion instability, in: 38th AIAA/ASME/SAE/ASEE Joint Propulsion Conference & Exhibit, 2002, p. 3578.

[23] G. Cai, Y. Zhang, H. Tian, P. Wang, N. Yu, Effect of grain port length–diameter ratio on combustion performance in hybrid rocket motors, Acta Astronaut. 128 (2016) 83–90.

[24] A. Karabeyoglu, "Lecture 10 Hybrid Rocket propulsion Design Issues," AA 284a Adv. Rocket Propulsion, AAE Dep. Stanford Univ., p. 18, 2012.

[25] R.D. Swami, A. Gany, Analysis and testing of similarity and scale effects in hybrid rocket motors, Acta Astronaut. 52 (8) (2003) 619–628.

[26] R.W. Humble, G.N. Henry, W.J. Larson, Space Propulsion Analysis and Design, Space Technology Series, McGraw-Hill, 1995.